

# Photonic Inverse Design of On-Chip Microresonators

Geun Ho Ahn, Ki Youl Yang, Rahul Trivedi, Alexander D. White, Logan Su, Jinhie Skarda, and Jelena Vučković\*



Cite This: <https://doi.org/10.1021/acsp Photonics.2c00020>



Read Online

ACCESS |



Metrics & More

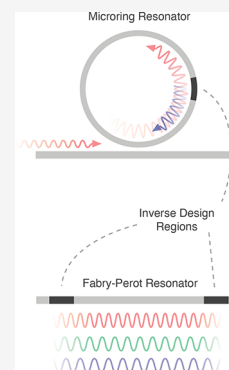


Article Recommendations



Supporting Information

**ABSTRACT:** The automation of device design enabled by optimization and machine learning techniques has been transformative for photonics. While this automation has been successful for nonresonant devices, automated photonic design has remained elusive for resonant devices, key elements for on-chip communication technologies of biosensing and quantum optics, due to their highly nonconvex optimization landscapes. We propose a framework that solves this problem by mapping the design of photonic resonators to a set of nonresonant design problems. We theoretically and experimentally demonstrate this framework and show flexible dispersion engineering, a quality factor beyond 2 million on silicon-on-insulator with single-mode operation, and selective wavelength-band operation.



**KEYWORDS:** microresonator, photonic inverse design, dispersion engineering, optical resonator, nonlinear optics

## INTRODUCTION

Optimization and machine learning in combination with large-scale electromagnetic simulations and rapid advances in high-performance computing hardware have enabled the automation of photonic design.<sup>1</sup> Furthermore, the development of lithographic fabrication technology for nanoscale structures has allowed for experimental implementation of the optimized designs even in commercial semiconductor foundries.<sup>2</sup> This automated design strategy, often called *inverse design*, begins with the construction of a cost function capturing the design target, expressed in terms of the electric field generated in the device. A gradient-based optimization algorithm is then used to efficiently explore a large space of devices and find the device that minimizes this cost function.

Most optimization algorithms, however, only find locally optimal solutions. Devices characterized by nonresonant field distributions, including but not limited to flat optical elements,<sup>3</sup> silicon photonics,<sup>4–6</sup> and accelerators on chip,<sup>7</sup> have many local optima that meet the design target and consequently have been successfully designed by these algorithms. On the other hand, the optimization landscape of resonant devices, which operate by confining electromagnetic fields in small spatial volumes, is much more complex and nonconvex. Therefore, its local optima do not meet the design target, making it harder to automate the design.<sup>8</sup> The current demonstrations of optimized resonators are restricted to either theoretical toy models in one and two dimensions<sup>9</sup> or three-dimensional devices that are difficult to fabricate and scale.<sup>10,11</sup> Since microresonators are vital in many applications, including but not limited to optical communication, biosensing, and

quantum technology,<sup>12–14</sup> a scalable automation of a microresonator design is expected to be broadly important.

Here, we address this problem by converting resonant device problems into a set of nonresonant device problems. Through this translation in the problem formulation, we demonstrate flexible engineering of the key performance metrics of a microresonator, such as optical quality factor,<sup>15–18</sup> dispersion,<sup>19–23</sup> and operational bandwidth.<sup>24–26</sup> This translation can be made possible, as those metrics of microresonators are dictated by the electromagnetic response of either the resonator boundary (for example, mirrors surrounding the resonator region) or the resonator volume. Hence the design specifications on the resonator can be translated to design specifications of the resonator boundary or the volume independently, which can be designed as entirely nonresonant device problems. This mapping effectively smooths the optimization landscape of the resonator design problem, opening it up to an application of automated design techniques that allow for co-engineering of multiple metrics within restricted fabrication constraints.

We demonstrate this framework theoretically and experimentally through three examples of resonator design, which appear in nonlinear optics,<sup>27–30</sup> and on-chip optical

Received: January 4, 2022

communication systems.<sup>31–33</sup> First we demonstrate a fine control over the resonant frequencies (i.e., dispersion) of both Fabry–Perot and microring resonators. Second, we demonstrate a high optical quality factor with a multimode waveguide while maintaining a single resonant mode family. Finally, we demonstrate the design of resonators with user-specified resonant wavelength bandwidths.

## RESULTS AND DISCUSSION

**Proposed Inverse Design Framework.** This proposed framework is schematically shown in Figure 1. In the case of

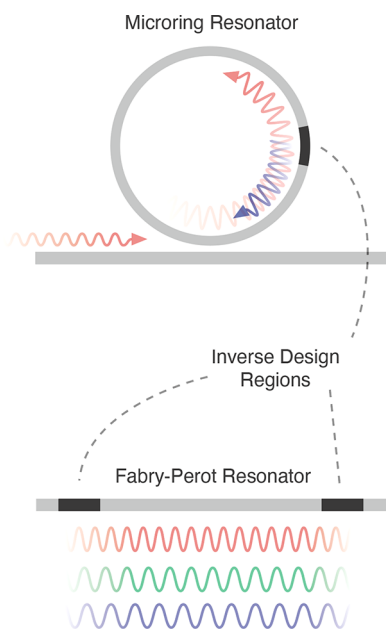


**Figure 1.** Schematic of inverse designed microring resonator and Fabry–Perot resonators with optimized elements inserted in the microresonator.

whispering gallery mode resonators such as microring resonators, we first develop an intracavity element framework to engineer the resonator property and provide an optimized intracavity element for the design targets. In the case of a Fabry–Perot resonator, the reflectors, which are used to form the resonator, are optimized with design targets needed for the microresonator engineering.

**Dispersion Engineering.** Whispering gallery mode resonators possess degenerate resonant modes that propagate in the clockwise and counterclockwise directions due to their cylindrical symmetry. By systematically coupling these two modes, we can control the positions of their resonances and engineer the desired dispersion profile. Therefore, we introduce inverse designed intracavity partially reflective elements (PREs)<sup>34</sup> to tailor the resonator properties. The PRE element is a nonresonant device and is therefore easily optimized for high performance. When this PRE is introduced in the resonator, it couples the counter propagating resonant modes, lifting the mode degeneracy. The coupling strength, which is dictated by the reflectivity of the element, determines the position of resonances of the resulting hybridized modes. More specifically, as we show in Supporting Information Section I, the resonance splitting between the hybridized modes is given by  $\Gamma = \theta/\pi \times \text{FSR}$ , where FSR is the free-spectral range of the resonator and  $\theta = \arctan(|r|/\sqrt{1 - |r|^2})$ ,

with  $|r|$  being the reflectance of the PRE at the resonant frequency of the unhybridized modes. Consequently, a desired microring dispersion, specified as the spectral position of resonant modes, can be translated to a frequency-dependent reflectance spectrum of the PRE, which can then be inverse designed. As a demonstration, we inverse design a PRE that has higher reflectance at higher frequency and lower reflectance at lower frequency. Figure 2a shows the scanning electron microscope (SEM) image of the inverse designed PRE embedded in a microring resonator fabricated on a silicon-on-insulator (SOI) platform. Figure 2b shows the transmission spectrum of the microring resonator. In this transmission spectrum, we observe that the splitting between the hybridized microring resonator modes and hence their resonant positions are dictated by the reflectance spectrum of the inverse designed PRE (Figure 2c). The measured integrated dispersion ( $D_{\text{int}}$ ) of the microring resonator with PRE is depicted in Figure 2d. We observe a clear correlation between the extent of mode splitting between the red-shifted and blue-shifted hybridized modes and the reflectance spectrum of the utilized PRE.

A similar inverse design technique can be applied to control the dispersion of on-chip Fabry–Perot (FP) resonators that are composed of two reflectors with a straight waveguide section in the middle. This length of waveguide,  $L_D$ , together with the group index  $n_g$  of the propagating waveguide mode controls the FSR of the microresonator, as  $\text{FSR} = c/2n_gL_D$ . Traditionally, the dispersion of the FP resonator is controlled by engineering the waveguide cross-section and the length of the waveguide.<sup>22</sup> Alternatively, more advanced reflector designs such as chirped mirrors are also employed to engineer the dispersion of FP resonators.<sup>35</sup> To achieve a finer spectral control over the dispersion of the resonator, we can alternatively use inverse design to engineer the frequency-dependent phase imparted by the mirrors at the ends of the FP resonator (Figure 3a). The FP resonator with inverse designed reflectors is schematically shown in Figure 3a. Notably, this concept of dispersion engineering using optimized reflectors with different dispersion targets is a generalization of chirped mirrors used in pulse engineering in lasers, where the distribution of multilayer coatings of thin films is optimized to provide engineered group delay dispersion.<sup>35</sup> As demonstrative examples, we use inverse designed reflectors to make the dispersion of FP resonators anomalous, where group velocity dispersion is positive, or normal, where group velocity dispersion is negative. In addition, the optimized reflectors can be very compact, with their width and length being only 0.5 and 3.0  $\mu\text{m}$ , respectively. The optimized dispersion engineered reflectors work by compensating the phase upon the reflection as targeted. Notably, the inverse design technique finds the optimal structure that provides the desired wavelength-dependent phase compensation in a compact footprint. Figure 3b illustrates the  $D_{\text{int}}$  of the microresonators formed by three different inverse designed reflectors with different dispersion targets, as shown in the SEM images of the reflectors in Figure 3c. The cavity length used here is 200  $\mu\text{m}$ . Figure 3b shows the tunable dispersion in equal length cavities ranging from anomalous to near-zero to normal, with  $D_2$  values ranging from 18 to  $-168$  MHz. In addition, the length of the cavities can be varied, achieving even more flexible dispersion engineering, as shown in Figure S2. To explore the potential implications of such dispersion engineered microresonators, we simulate optical parametric oscillation (OPO) based on the

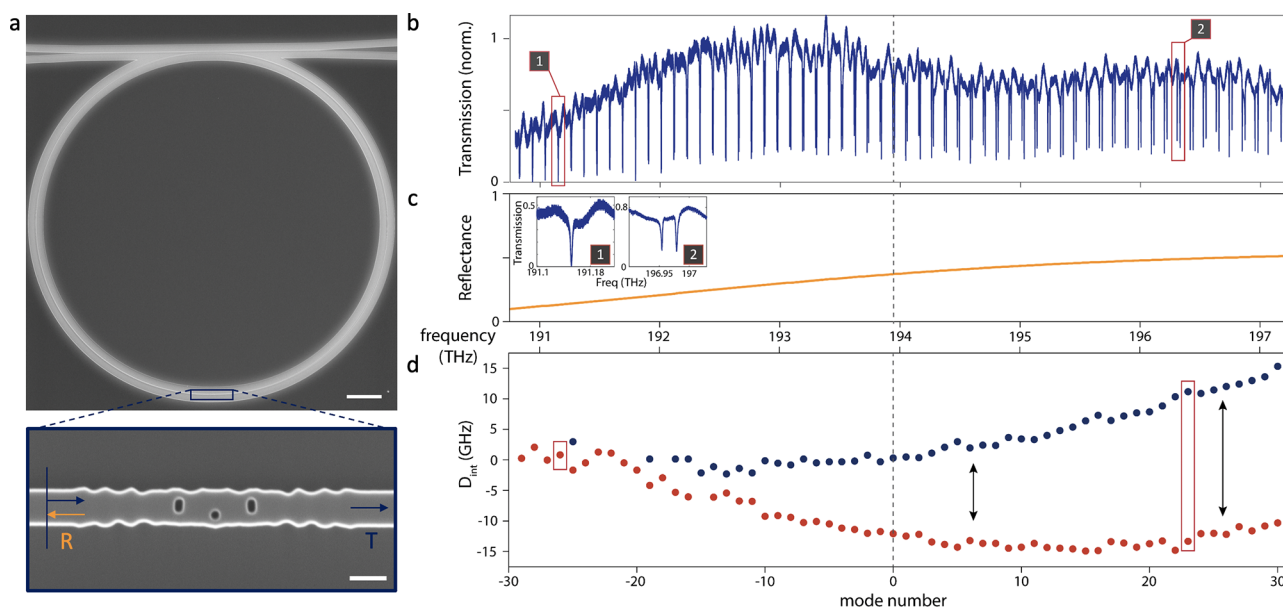


**Figure 2.** Inverse designed intracavity element for microring resonator frequency engineering. (a) SEM of a fabricated Si microring resonator with the partially reflective element in the microring. The microring resonator is designed with a ring radius of 100 μm, and the width of the waveguide is 500 nm. The scale bar here is 20 μm and 500 nm, respectively. (b) Transmission spectrum of the fabricated device with the inverse designed intracavity element. (c) Simulated reflectance spectrum of the corresponding inverse designed intracavity element with increasing reflectance as frequency increases. (d) Measured integrated dispersion of the split fundamental modes, indicated by blue and red points for each side of the split modes.

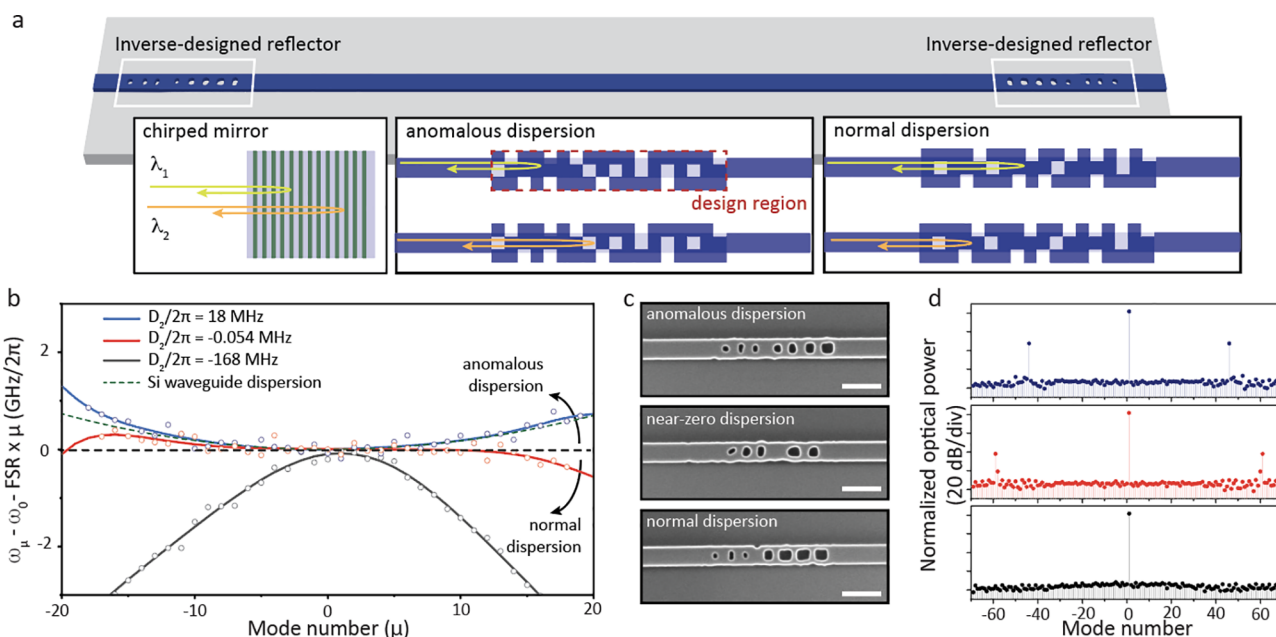


**Figure 3.** Inverse designed dispersion engineered Fabry–Perot resonators. (a) Schematic of inverse designed FP resonator and conceptual depiction of dispersion compensation from the inverse designed reflectors, analogous to chirped mirrors. (b) Measured integrated dispersion of three inverse designed FP resonators with a cavity length of 200 μm with inverse designed reflectors with dispersion targets. Blue, red, and black lines correspond to fit lines for the three FP resonators, showing anomalous, near-zero, and normal dispersion. (c) SEM images of the three different inverse designed reflectors used for the dispersion engineered resonators. (d) OPO simulation of the FP resonator with the experimental dispersion coefficients  $D_2$  and  $D_3$  derived from dispersion measurements of the three FP resonators with a cavity length of 480 μm.

experimentally derived dispersion coefficients. The detailed implementation of the OPO simulation of a Fabry–Perot resonator with two photon absorption of silicon is shown in Supporting Information Section II. Figure 3d shows the result of OPO simulations with three different dispersion profiles derived from the inverse designed FP resonators with a 480 μm cavity length, shown in Figure S2. Importantly, when

the dispersion of the microresonator is engineered to be normal, we do not see any OPO sideband generation, as expected. When the dispersion of the microresonator is engineered to be anomalous at different strengths, the microresonators show OPOs generated at different resonance modes.

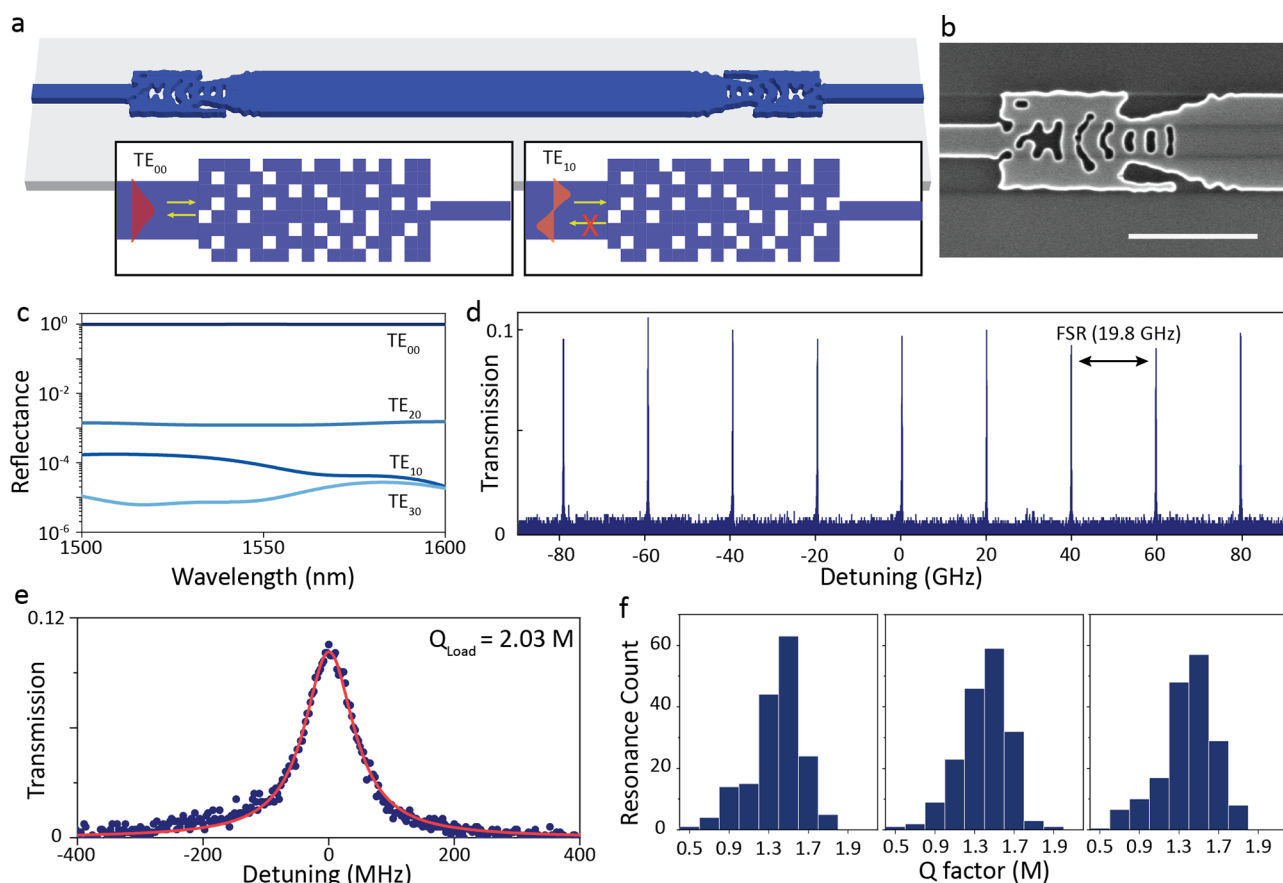


**Figure 4.** Inverse design of a high- $Q$  FP resonator with single-mode operation. (a) Schematic of the inverse designed FP resonator with inverse designed multimode reflectors allowing for a wide width waveguide for the resonator and single-mode waveguide outputs. Conceptual picture showing the functionality of the reflector, as it reflects the fundamental mode well and can couple out the fundamental mode, while other higher order modes are not supported. (b) SEM image of the single-mode inverse designed reflector with a wider width waveguide ( $1.5\ \mu\text{m}$ ) for reflection of the fundamental mode. A single-mode waveguide of  $0.5\ \mu\text{m}$  width is used on the other side to couple out the resonances from the resonator. The scale bar is  $2\ \mu\text{m}$ . (c) Simulated reflectance of the depicted inverse design reflector when excited with different TE modes, showing its selective reflection of the fundamental mode only. (d) Zoomed-in transmission spectrum through the FP resonator, showing single-mode operation separated by an FSR of  $19.8\ \text{GHz}$ . (e)  $Q$ -factor fit of a resonance of the inverse designed FP resonator, showing a loaded  $Q$ -factor of  $2.03\ \text{M}$ . The transmission value of the resonance is  $0.101$ . (f)  $Q$ -factor statistics of the resonance distribution from three different fabrication runs of identical FP resonator design.

**Optical Quality Factor Engineering.** To achieve microresonators with a high optical quality factor, reduction of scattering losses from the waveguide surface roughness is crucial. Typically, this is done by reducing the interaction between the optical field and the surface of the microresonator. In the design process, this can be achieved by using thicker and wider width waveguides that support a very well confined waveguide mode.<sup>31</sup> However, wider waveguides often support multiple higher order waveguide modes that can introduce coupling between different mode families.<sup>36</sup> Therefore, a low-loss microresonator that supports only the fundamental mode is desired. We utilize photonic inverse design to achieve this goal. We optimize reflectors that selectively reflect only the fundamental mode of the wide waveguide and couple the transmitted field directly to a single-mode waveguide. This mode-selective reflector suppresses higher order modes, as schematically shown in Figure 4a. Figure 4b shows the SEM of the inverse designed reflector fabricated on a SOI stack, and Figure 4c shows its simulated reflectance when excited with different waveguide modes. We clearly see that the reflector acts as a near-perfect mirror only for the fundamental waveguide mode, while the remaining waveguide modes are

allowed to transmit through and hence do not interfere with the fundamental mode operation. Furthermore, this functionality is achieved with a device footprint of  $3.5\ \mu\text{m}$  by  $1.5\ \mu\text{m}$ , which is significantly smaller than the conventional mode tapers that can be used to accomplish the similar task within the ring.<sup>36</sup> Figure 4d shows the transmission spectrum of the FP resonator, verifying the FP resonator operates only with a single mode. Figure 4e shows the zoomed-in spectrum of a single resonator mode, showing that the inverse designed FP resonator experimentally achieves a loaded  $Q$ -factor of  $2.03$  million at telecommunication wavelengths in the foundry-compatible SOI system. Furthermore, the design is robust to the fabrication variation. In Figure 4f, we measure the  $Q$ -factor of different fabrication runs of the same FP resonator design and consistently achieve high- $Q$ -factor operations.

**Selective Resonance Bands.** The last design problem that we address is supporting a microresonator with resonant frequencies in selective frequency bands. One possible application of such a device is to reduce the pump power leakage into undesired modes during a nonlinear wave mixing process. This nonlinear parasitic coupling decreases conversion efficiency from the mode competition process.<sup>37,38</sup> This is

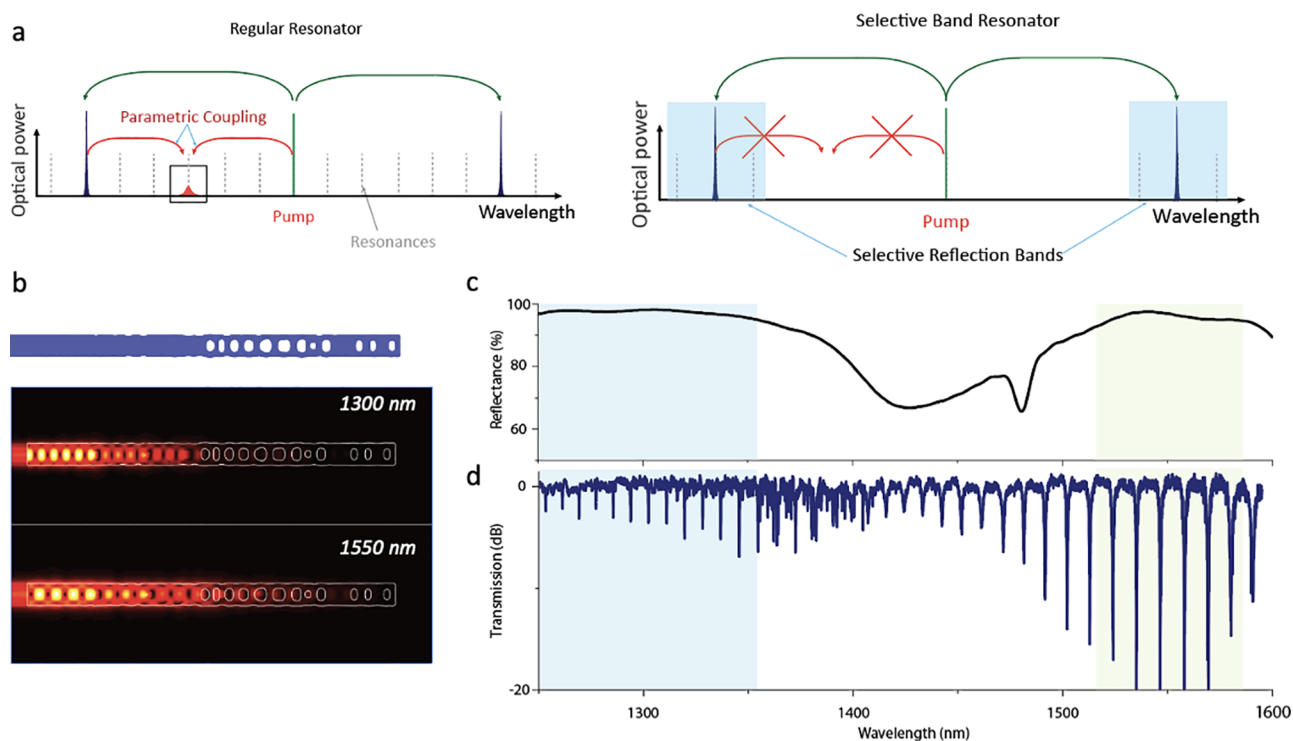


**Figure 5.** Inverse design of a selective wavelength band resonator. (a) Graphical representation of parametric coupling in a typical resonator and in a selective band resonator, formed by selective reflection bands. (b) Schematic of a utilized inverse designed selective wavelength reflector and its simulated electric field profile at the chosen wavelength of operation (1300 and 1550 nm). (c) Simulated reflectance profile of the inverse designed selective reflection band reflector, showing high reflectance at the O-band and C-band with low reflectance in other wavelength bands. (d) Measured transmission spectrum of the selective wavelength band resonator, showing sharp resonances in both the O-band and C-band, while the resonances outside these bands are broad.

schematically depicted in Figure 5a, wherein we contrast between parametric down-conversion in a regular resonator, where coupling to many undesired resonant modes is possible. On the other hand, in a frequency band-selective resonator, such couplings are absent. To achieve this with FP resonators, we can utilize a photonic inverse design to optimize for a high reflectance at chosen wavelength bands and suppress the reflection at undesired wavelength bands. As a demonstration, we optimize a silicon reflector that has a high reflectance at 1300 and 1550 nm wavelength bands, which correspond to the O-band and C-band, and reflectance suppression in the middle band (1410 nm). The resulting inverse-designed device, with a footprint of  $8 \mu\text{m} \times 0.5 \mu\text{m}$ , is shown in Figure 5b, along with its simulated electric field profiles at the selected wavelengths. As shown in the electric field profiles, the single mirror reflects two well-separated wavelengths (1300 and 1550 nm) effectively; its simulated reflectance spectrum is shown in Figure 5c. The schematic of the FP formed by the reflector is shown in Figure S3. To optically characterize the resonator, we side couple the resonator to a waveguide-cavity directional coupler. We note the difficulty in coupling equally to a resonator across distant wavelength bands.<sup>30</sup> Therefore, the resonance in the O-band is weakly coupled, while the resonance in the C-band is close to critically coupled. This can be mediated by engineering coupler designs further.<sup>30</sup> Figure 5d depicts the measured transmission spectrum of the selective wavelength band microresonator. This resonator can achieve a moderate loaded  $Q$ -factor in both of the selected bands ( $Q = 1.5\text{--}7K$ ), while the suppressed wavelength bands show a loaded quality factor as low as 600, which provides

more than an order of magnitude difference between the selected and suppressed wavelength bands.

## CONCLUSION

In summary, we utilize nonresonant device optimizations for on-chip microresonator designs that enable flexible engineering of important figures of merit, such as dispersion  $Q$ -factor and selective wavelength band operation. As the proposed framework can co-engineer multiple key metrics, we foresee the combination of these techniques to have broad applicability. An immediate application of our approach would be microresonator designs in other material platforms. For instance, band-selective microresonators can be designed in materials with a high second-order nonlinearity, such as lithium niobate<sup>39</sup> and silicon carbide,<sup>40</sup> for second-harmonic generations in visible and telecom wavelength bands. In silicon, foundry fabricable near-zero dispersion resonators open up the possibility of resonator-enhanced electro-optic modulator combs<sup>28,29</sup> and mid-IR nonlinear wave mixing,<sup>41</sup> which is critical for on-chip communications and spectroscopy.

## METHODS

**Photonic Inverse Design.** Stanford Photonics Inverse Design Software (SPINS) was utilized to optimize the various reflectors and the intracavity element shown throughout the work. SPINS can provide the design of various on-chip elements as previously demonstrated.<sup>4,34,42</sup> An open source version of the software package is available.<sup>42</sup> The objective function formulation used throughout this paper is  $f_{\text{obj}}(\epsilon) = (1 - |c^\dagger E(\epsilon)|)^2$ , where  $|c^\dagger E(\epsilon)|$  computes the modal overlap of the

vectorized electric field  $E$  in the device with the target back-reflected fundamental mode  $c$ . We then minimize this objective function during the optimization. Typically the optimization required 200 iterations in the continuous and discrete optimization phases to reach final designs.

**Device Fabrication.** The inverse designed resonator devices were fabricated on silicon-on-insulator with 220 nm silicon device layer thickness with underlying buried oxide with a 2  $\mu\text{m}$  thickness. The patterns for device have been written with a JEOL JBX-6300FS electron-beam lithography system with ZEP520A as the resist. After the development of the pattern, HBr/O<sub>2</sub>/He plasma etching was used to etch the silicon layer. Solvent bath and piranha cleaning were used to remove the e-beam resist.

## ■ ASSOCIATED CONTENT

### SI Supporting Information

The Supporting Information is available free of charge at <https://pubs.acs.org/doi/10.1021/acsp Photonics.2c00020>.

Details on modeling a partially reflecting element in microring resonators; modeling two-photon absorption in optical parametric oscillation simulations; supporting figures (PDF)

## ■ AUTHOR INFORMATION

### Corresponding Author

Jelena Vučković – E. L. Ginzton Laboratory, Stanford University, Stanford, California 94305, United States; Email: [jela@stanford.edu](mailto:jela@stanford.edu)

### Authors

Geun Ho Ahn – E. L. Ginzton Laboratory, Stanford University, Stanford, California 94305, United States; [orcid.org/0000-0002-4761-7804](https://orcid.org/0000-0002-4761-7804)

Ki Youl Yang – E. L. Ginzton Laboratory, Stanford University, Stanford, California 94305, United States; [orcid.org/0000-0002-0587-3201](https://orcid.org/0000-0002-0587-3201)

Rahul Trivedi – E. L. Ginzton Laboratory, Stanford University, Stanford, California 94305, United States; Max-Planck-Institut für Quantenoptik, 85748 Garching, Germany

Alexander D. White – E. L. Ginzton Laboratory, Stanford University, Stanford, California 94305, United States; [orcid.org/0000-0002-5387-310X](https://orcid.org/0000-0002-5387-310X)

Logan Su – E. L. Ginzton Laboratory, Stanford University, Stanford, California 94305, United States; [orcid.org/0000-0002-4050-7338](https://orcid.org/0000-0002-4050-7338)

Jinhie Skarda – E. L. Ginzton Laboratory, Stanford University, Stanford, California 94305, United States; [orcid.org/0000-0003-0785-4984](https://orcid.org/0000-0003-0785-4984)

Complete contact information is available at: <https://pubs.acs.org/doi/10.1021/acsp Photonics.2c00020>

### Notes

The authors declare no competing financial interest.

## ■ ACKNOWLEDGMENTS

We acknowledge insightful discussions with F. Aflatouni, S. Papp, and K. Srinivasan. We thank G. Keeler and the program management teams for discussions throughout the project. G.H.A. acknowledges support from STMicroelectronics Stanford Graduate Fellowship (SGF) and Kwanjeong Educational Foundation. R.T. acknowledges Max Planck Harvard

Research Center for a quantum optics (MPHQ) postdoctoral fellowship. A.W. acknowledges the Herb and Jane Dwight Stanford Graduate Fellowship and the NTT Research Fellowship. J.S. acknowledges support from Cisco Systems Stanford Graduate Fellowship (SGF). This work is funded by the DARPA under the PIPES and LUMOS program.

## ■ REFERENCES

- (1) Molesky, S.; Lin, Z.; Piggott, A. Y.; Jin, W.; Vucković, J.; Rodriguez, A. W. Inverse design in nanophotonics. *Nat. Photonics* **2018**, *12*, 659–670.
- (2) Piggott, A. Y.; Ma, E. Y.; Su, L.; Ahn, G. H.; Sapra, N. V.; Vercruyse, D.; Netherton, A. M.; Khope, A. S.; Bowers, J. E.; Vuckovic, J. Inverse-designed photonics for semiconductor foundries. *ACS Photonics* **2020**, *7*, 569–575.
- (3) Zhou, M.; Liu, D.; Belling, S. W.; Cheng, H.; Kats, M. A.; Fan, S.; Povinelli, M. L.; Yu, Z. Inverse Design of Metasurfaces Based on Coupled-Mode Theory and Adjoint Optimization. *ACS Photonics* **2021**, *8*, 2265–2273.
- (4) Su, L.; Trivedi, R.; Sapra, V. N.; Piggott, Y. A.; Vercruyse, D.; Vucković, J. Fully-automated optimization of grating couplers. *Opt. Express* **2018**, *26*, 4023–4034.
- (5) Callewaert, F.; Butun, S.; Li, Z.; Aydin, K. Inverse design of an ultra-compact broadband optical diode based on asymmetric spatial mode conversion. *Sci. Rep.* **2016**, *6*, 32577.
- (6) Piggott, A. Y.; Lu, J.; Lagoudakis, K. G.; Petykiewicz, J.; Babinec, T. M.; Vučković, J. Inverse design and demonstration of a compact and broadband on-chip wavelength demultiplexer. *Nat. Photonics* **2015**, *9*, 374–377.
- (7) Sapra, N. V.; Yang, K. Y.; Vercruyse, D.; Leedle, K. J.; Black, D. S.; England, R. J.; Su, L.; Trivedi, R.; Miao, Y.; Solgaard, O.; Byer, R. L.; Vučković, J. On-chip integrated laser-driven particle accelerator. *Science* **2020**, *367*, 79–83.
- (8) Trivedi, R. Gradient descent globally solves average-case non-resonant physical design problems. November 4, 2021, *arXiv*, 2111.02978 (accessed 2021–11–08).
- (9) Lin, Z.; Liang, X.; Lončar, M.; Johnson, S. G.; Rodriguez, A. W. Cavity-enhanced second-harmonic generation via nonlinear-overlap optimization. *Optica* **2016**, *3*, 233–238.
- (10) Lu, J.; Boyd, S.; Vučković, J. Inverse design of a three-dimensional nanophotonic resonator. *Opt. Express* **2011**, *19*, 10563–10570.
- (11) Liang, X.; Johnson, S. G. Formulation for scalable optimization of microcavities via the frequency-averaged local density of states. *Opt. Express* **2013**, *21*, 30812–30841.
- (12) Vahala, K. J. Optical microcavities. *Nature* **2003**, *424*, 839–846.
- (13) Xu, Q.; Schmidt, B.; Pradhan, S.; Lipson, M. Micrometre-scale silicon electro-optic modulator. *Nature* **2005**, *435*, 325–327.
- (14) Englund, D.; Fattal, D.; Waks, E.; Solomon, G.; Zhang, B.; Nakaoka, T.; Arakawa, Y.; Yamamoto, Y.; Vučković, J. Controlling the spontaneous emission rate of single quantum dots in a two-dimensional photonic crystal. *Phys. Rev. Lett.* **2005**, *95*, 013904.
- (15) Jin, W.; Yang, Q.-F.; Chang, L.; Shen, B.; Wang, H.; Leal, M. A.; Wu, L.; Gao, M.; Feshali, A.; Paniccia, M.; et al. Hertz-linewidth semiconductor lasers using CMOS-ready ultra-high-Q microresonators. *Nat. Photonics* **2021**, *15*, 346–353.
- (16) Puckett, M. W.; Liu, K.; Chauhan, N.; Zhao, Q.; Jin, N.; Cheng, H.; Wu, J.; Behunin, R. O.; Rakich, P. T.; Nelson, K. D.; et al. 422 Million intrinsic quality factor planar integrated all-waveguide resonator with sub-MHz linewidth. *Nat. Commun.* **2021**, *12*, 1–8.
- (17) Yang, K. Y.; Oh, D. Y.; Lee, S. H.; Yang, Q.-F.; Yi, X.; Shen, B.; Wang, H.; Vahala, K. Bridging ultrahigh-Q devices and photonic circuits. *Nat. Photonics* **2018**, *12*, 297–302.
- (18) Pfeiffer, M. H.; Liu, J.; Raja, A. S.; Morais, T.; Ghadiani, B.; Kippenberg, T. J. Ultra-smooth silicon nitride waveguides based on the Damascene reflow process: fabrication and loss origins. *Optica* **2018**, *5*, 884–892.

- (19) Okawachi, Y.; Lamont, M. R.; Luke, K.; Carvalho, D. O.; Yu, M.; Lipson, M.; Gaeta, A. L. Bandwidth shaping of microresonator-based frequency combs via dispersion engineering. *Opt. Lett.* **2014**, *39*, 3535–3538.
- (20) Yang, K. Y.; Beha, K.; Cole, D. C.; Yi, X.; Del'Haye, P.; Lee, H.; Li, J.; Oh, D. Y.; Diddams, S. A.; Papp, S. B.; et al. Broadband dispersion-engineered microresonator on a chip. *Nat. Photonics* **2016**, *10*, 316–320.
- (21) Kim, S.; Han, K.; Wang, C.; Jaramillo-Villegas, J. A.; Xue, X.; Bao, C.; Xuan, Y.; Leaird, D. E.; Weiner, A. M.; Qi, M. Dispersion engineering and frequency comb generation in thin silicon nitride concentric microresonators. *Nat. Commun.* **2017**, *8*, 1–8.
- (22) Yu, S.-P.; Jung, H.; Briles, T. C.; Srinivasan, K.; Papp, S. B. Photonic-crystal-reflector nanoresonators for Kerr-frequency combs. *ACS Photonics* **2019**, *6*, 2083–2089.
- (23) Zhang, Z.; Norman, J. C.; Liu, S.; Malik, A.; Bowers, J. E. Integrated dispersion compensated mode-locked quantum dot laser. *Photonics Res.* **2020**, *8*, 1428–1434.
- (24) Liu, X.; Bruch, A. W.; Gong, Z.; Lu, J.; Surya, J. B.; Zhang, L.; Wang, J.; Yan, J.; Tang, H. X. Ultra-high-Q UV microring resonators based on a single-crystalline AlN platform. *Optica* **2018**, *5*, 1279–1282.
- (25) Desiatov, B.; Shams-Ansari, A.; Zhang, M.; Wang, C.; Lončar, M. Ultra-low-loss integrated visible photonics using thin-film lithium niobate. *Optica* **2019**, *6*, 380–384.
- (26) Griffith, A. G.; Lau, R. K.; Cardenas, J.; Okawachi, Y.; Mohanty, A.; Fain, R.; Lee, Y. H. D.; Yu, M.; Phare, C. T.; Poitras, C. B.; et al. Silicon-chip mid-infrared frequency comb generation. *Nat. Commun.* **2015**, *6*, 1–5.
- (27) Kippenberg, T. J.; Gaeta, A. L.; Lipson, M.; Gorodetsky, M. L. Dissipative Kerr solitons in optical microresonators. *Science* **2018**, *361*, eaan8083.
- (28) Zhang, M.; Buscaino, B.; Wang, C.; Shams-Ansari, A.; Reimer, C.; Zhu, R.; Kahn, J. M.; Lončar, M. Broadband electro-optic frequency comb generation in a lithium niobate microring resonator. *Nature* **2019**, *568*, 373–377.
- (29) Idjadi, M. H.; Arab, S.; Aflatouni, F. Optical Frequency Comb Generation in Silicon by Recursive Electro-Optic Modulation. *CLEO: Science and Innovations* **2020**, SF3O–5.
- (30) Lu, X.; Moille, G.; Li, Q.; Westly, D. A.; Singh, A.; Rao, A.; Yu, S.-P.; Papp, S. B.; Srinivasan, K. Efficient telecom-to-visible spectral translation through ultralow power nonlinear nanophotonics. *Nat. Photonics* **2019**, *13*, 593–601.
- (31) Biberman, A.; Shaw, M. J.; Timurdogan, E.; Wright, J. B.; Watts, M. R. Ultralow-loss silicon ring resonators. *Opt. Lett.* **2012**, *37*, 4236–4238.
- (32) Timurdogan, E.; Sorace-Agaskar, C. M.; Sun, J.; Hosseini, E. S.; Biberman, A.; Watts, M. R. An ultralow power athermal silicon modulator. *Nat. Commun.* **2014**, *5*, 1–11.
- (33) Atabaki, A. H.; Moazeni, S.; Pavanello, F.; Gevorgyan, H.; Notaros, J.; Alloatti, L.; Wade, M. T.; Sun, C.; Kruger, S. A.; Meng, H.; et al. Integrating photonics with silicon nanoelectronics for the next generation of systems on a chip. *Nature* **2018**, *556*, 349–354.
- (34) Yang, K. Y.; Skarda, J.; Cotrufo, M.; Dutt, A.; Ahn, G. H.; Sawaby, M.; Vercruyse, D.; Arbabian, A.; Fan, S.; Alu, A.; et al. Inverse-designed non-reciprocal pulse router for chip-based LiDAR. *Nat. Photonics* **2020**, *14*, 369–374.
- (35) Szpöcs, R.; Ferencz, K.; Spielmann, C.; Krausz, F. Chirped multilayer coatings for broadband dispersion control in femtosecond lasers. *Opt. Lett.* **2020**, *8*, 1676–1686.
- (36) Kordts, A.; Pfeiffer, M. H. P.; Guo, H.; Brasch, V.; Kippenberg, T. J. Higher order mode suppression in high-Q anomalous dispersion SiN microresonators for temporal dissipative Kerr soliton formation. *Opt. Lett.* **2016**, *41*, 452–455.
- (37) McKenna, T. P.; Stokowski, H. S.; Ansari, V.; Mishra, J.; Jankowski, M.; Sarabalis, C. J.; Herrmann, J. F.; Langrock, C.; Fejer, M. M.; Safavi-Naeini, A. H. Ultra-low-power second-order nonlinear optics on a chip. February 10, 2021, *arXiv*, 2102.05617 (accessed 2021–09–14).
- (38) Stone, J. R.; Moille, G.; Lu, X.; Srinivasan, K. Conversion Efficiency in Kerr-Microresonator Optical Parametric Oscillators: From Three Modes to Many Modes. *Phys. Rev. Applied* **2022**, *17*, 024038.
- (39) Wang, C.; Zhang, M.; Chen, X.; Bertrand, M.; Shams-Ansari, A.; Chandrasekhar, S.; Winzer, P.; Lončar, M. Integrated lithium niobate electro-optic modulators operating at CMOS-compatible voltages. *Nature* **2018**, *562*, 101–104.
- (40) Lukin, D. M.; Dory, C.; Guidry, M. A.; Yang, K. Y.; Mishra, S. D.; Trivedi, R.; Radulaski, M.; Sun, S.; Vercruyse, D.; Ahn, G. H.; et al. 4H-silicon-carbide-on-insulator for integrated quantum and nonlinear photonics. *Nat. Photonics* **2020**, *14*, 330–334.
- (41) Runge, A. F. J.; Hudson, D. D.; Tam, K. K. K.; de Sterke, C. M.; Blanco-Redondo, A. The pure-quartic soliton laser. *Nat. Photonics* **2020**, *14*, 492–497.
- (42) Su, L.; Vercruyse, D.; Skarda, J.; Sapra, N. V.; Petykiewicz, J. A.; Vučković, J. Nanophotonic inverse design with SPINS: Software architecture and practical considerations. *Appl. Phys. Rev.* **2020**, *7*, 011407.